Biointerface Research in Applied Chemistry
Open-Access Journal (ISSN: 2069-5837)

Article
Volume 15, Issue 5, 2025, 61
https://doi.org/10.33263/BRIAC155.061

Development and Analysis of Glycine-Modified Silica Gel for Efficient Fe^{3+} Ion Capture: Exploring Synchrotron XAFS Insights

Mohammed A. Al-Anber [1,*], Messaoud Harfouche [2], Ahmed K. Hijazi [3,4], Dinara Sobola [5,6], Mo'tasem Al-Bayed [4], Neda'a Al-Adaileh [7], Suresh Sagadevan [7]

1 Department of Chemistry, Faculty of Sciences, Applied Science Private University, P.O. Box 541350, 11937 Amman, Jordan
2 Synchrotron-light for Experimental Science and Applications in the Middle East (SESAME), Allan 19252, Jordan
3 Department of Chemistry, College of Arts and Sciences, University of Petra, P.O. Box 961343, Amman 11196, Jordan
4 Department of Chemical Sciences, Faculty of Arts and Science, Jordan University of Science and Technology, Irbid, Jordan
5 Department of Physics, Faculty of Electrical Engineering and Communication, Brno University of Technology, Technical 10, 616 00 Brno, Czech Republic
6 Institute of Physics of Materials, Czech Academy of Sciences, Žižkova 22, 61662 Brno, Czech Republic
7 Nanotechnology and Catalysis Research Centre, University of Malaya, Kuala Lumpur 50603, Malaysia
* Correspondence: m_alanber@ASU.edu.jo;

Received: 13.02.2025; Accepted: 24.07.2025; Published: 9.05.2025

Abstract: A glycine-functionalized silica gel material (SG-Gly-Na^+) was synthesized via a sol–gel approach for efficient Fe^{3+} ion removal from aqueous solutions. Characterization by ATR-FTIR, SEM, elemental analysis, and synchrotron-based X-ray absorption spectroscopy confirmed the successful incorporation of glycine and the structural integrity of the silica matrix. FTIR and thermal analysis validated the presence of carboxylate and secondary amine groups and demonstrated thermal stability up to 350°C. XANES analysis revealed that iron remains in the +3 oxidation state upon sorption, while EXAFS indicated coordination of Fe^{3+} to oxygen atoms at ~1.95 Å, with longer-range interactions involving the silica framework. Notably, the glycine moiety does not reduce Fe(III) within the matrix. Batch sorption tests showed that SG-Gly-Na^+ achieved 70% Fe^{3+} removal efficiency, a significant improvement over unmodified silica gel (10%), demonstrating its potential as a selective and thermally stable sorbent for iron remediation.

Keywords: silica gel; glycine; amino acids; Fe^{3+} ion; sorption; synchrotron XAFS.

1. Introduction

Silica gel (SG) and its organically modified derivatives are widely used for removing heavy metal ions from wastewater due to their tunable surface functionality and high stability [1, 2]. Functionalization with amino acids such as glycine, diglycine, or triglycine has led to enhanced sorption properties. For instance, glycine-modified silica has shown high selectivity and capacity for Cu^{2+} and Fe^{3+} ions [3–5]. Other surface-modified silica gels, including those incorporating tris(2-aminoethyl)amine or L-glutamic acid, have also demonstrated improved metal ion capture efficiency for U(VI), Zn^{2+}, and Fe^{2+} under varying conditions [4–7]. Notably,

glycine-modified mesoporous silica prepared through two-step methods has exhibited strong affinity for Co^{2+} and Ni^{2+} ions, attributed to surface localization of glycine groups [8]. Building on these findings, the present work aims to synthesize and characterize glycine-functionalized silica gel (SG-$Gly^{-}Na^{+}$) using a sol–gel approach. Characterization is performed using FTIR, PXRD, elemental analysis, SEM, and thermal analyses (TGA and DSC). The material's ability to capture Fe^{3+} ions from aqueous solutions is then evaluated using batch sorption experiments. Recent reports suggest glycine may also act as a reducing agent for metal ions [9], prompting further investigation into the oxidation state and coordination environment of Fe in the SG-$Gly^{-}Na^{+}$ system. To this end, synchrotron-based X-ray absorption spectroscopy, including X-ray Absorption Near-Edge Structure (XANES) and Extended X-ray Absorption Fine Structure (EXAFS), is employed. Although EXAFS has previously been applied to study metal environments in sol-gel systems, this study uniquely combines both XANES and EXAFS to probe Fe(III) speciation and its interaction with glycine-functionalized silica at the atomic level.

2. Materials and Methods

2.1. Reagents.

Iron(III) nitrate [$Fe(NO_3)_3 \cdot 9H_2O$] (Fluka Chemika, Germany), 1,3-chloropropyltrimethoxysilane (CPTMS), glycine (G), sodium hydroxide, and ethanol (Sigma-Aldrich, Germany) were all of analytical reagent grade and were used without further purification. A stock solution (1000 mg/L) of Fe^{3+} ions is prepared by dissolving a stoichiometric amount of $Fe(NO_3)_3 \cdot 9H_2O$ in 1000 mL of ultrapure deionized water (18 MΩ·cm). Standard model solutions ranging from 1–100 mg/L are prepared by serial dilution.

2.2. Instrumentation and analysis.

The concentration of Fe^{3+} ions in aqueous solution is determined using a spectrophotometer (Varian Spectra AA 55, Perkin-Elmer, USA). Elemental analysis (EA) is used to determine elemental composition (CHNSO, Belgium). Powder X-ray diffraction (p-XRD) (Rigaku, Japan) is employed to characterize the new material. The pH of all solutions is measured using a pH meter (Milwaukee MI 150, Romania). A temperature controller and an isothermal shaker (Memmert, Germany) are used to maintain constant temperature. Thermogravimetric analysis (TGA) and differential scanning calorimetry (DSC) (Linseis, Germany) are conducted to investigate the thermal stability of SG-Gly–Na^{+}. The analytical balance is calibrated to ±0.0001 g (Sartorius, CP324-S, ISO 9001 management system). Melting points are determined using a Gallenkamp MFB 595 010M melting point apparatus with analytically pure samples sealed in nitrogen-purged capillaries. For the synthesized powders, infrared spectra in the range of 400–4000 cm^{-1} are recorded using attenuated total reflectance infrared spectroscopy (ATR-IR, BRUKER, Germany).

Using the BM08-XAFS/XRF beamline of the Synchrotron-light for Experimental Science and Applications in the Middle East (SESAME) [10], Fe K-edge XAFS spectra are acquired at ambient room temperature. A double-crystal monochromator equipped with a Si (111) crystal is used to tune the energy for a step-by-step scan, achieving an energy resolution (ΔE) of ~0.2 eV. Higher harmonics are effectively rejected thanks to the Si-coated stripe on the optics' collimating and focusing mirrors. The sample XAFS spectra are collected at ambient temperature in fluorescence mode using a silicon drift detector (SDD).

XAFS data are processed and analyzed using the standard WinXAS software package [11]. The spectra are subjected to background subtraction, normalization, energy conversion into k, weighting, and Fourier filtering. The threshold energy (E_0) is defined as the first inflection point where the second derivative vanishes.

k3-weighted EXAFS signals were Fourier transformed using a Hanning window function for a wavenumber ranging between 2.5-11.0 $Å^{-1}$ for all references and SG-Gly. However, the WinXAS software package was used to model and structurally fit the collected EXAFS signal. The best data to fit structural parameters were extracted from EXAFS fitting by applying theoretical structural EXAFS models of FeO, Fe_2O_3, and $FeSiO_3$ calculated using the FEFF code [12] based on "cif" files generated from the crystallography data. Considering the well-known EXAFS equation, the fitting parameters, except for the amplitude reduction factor ($S02$), were set variables for all scattering paths. The amplitude reduction factor ($S02$) was determined to be 0.9 from the fitting of Fe foil EXAFS data collected in the same experimental conditions as the samples. Correlations between the fitting parameters were used as a checking tool for the type of backscattering atoms as well as the goodness of the fits.

The powder X-ray Diffraction (p-XRD) data are analyzed with a GBC EMMA and CuKα radiation X-ray diffractometer at a 25 kV acceleration voltage and 400 µA current. The diffraction angle is scanned at a rate of 4.00°/minute from 2θ = 15° to 60°.

2.3. Synthesis of glycine-functionalized silica gel (4: SG-Gly-Na^+).

In summary, the sol-gel method is selected for its versatility, ability to produce nanoscale materials, and suitability for synthesizing hybrid materials with controlled properties. The resulting SG-Gly–Na^+ material is expected to exhibit specific characteristics desirable for the intended application. The sol-gel method is applied in a one-pot reaction with glycine (Gly: 2.25 g, 30.0 mmol) and sodium hydroxide (1.2 g, 30.0 mmol) dissolved in a 20 mL mixture of distilled water and 6 mL of ethanol. At T = 25°C and pH = 13, the reaction is stirred for t = 10 minutes. 1,3-Chloropropyltrimethoxysilane (CPTMS: 5.47 mL, 30.0 mmol) is added dropwise over 15 minutes while vigorously stirring. After a few minutes, the color of the solution gradually changes from colorless to milky. After 15 minutes, the sticky precipitate transforms into a brittle white solid. Upon completion, the reaction mixture is left at room temperature for two days. Subsequently, it is filtered and washed with ethanol and distilled water. The obtained solids are dried for 3 hours at 75°C using a rotary evaporator. The resulting white SG-Gly–Na^+solid is crushed into a fine powder (75–250 µm) using a mortar and pestle. The SG-Gly–Na^+ particles are washed with ethanol and then distilled water (5 mL × 3) to remove excess Gly-Na^+. The adsorbed solvent is removed under vacuum over several days, yielding the final product: Yield = 2.7 g (57 %). M.p. (decom.) 240°C. ATR-FT-IR (KBr pellet): 3385 cm^{-1} (m, ν2ed N-H); 1592 cm^{-1} (ν ν2ed N-H bending); 1562 cm^{-1} (s, νenol C=O); 1495 cm^{-1} (s, νC-O); 1017 and 1101 cm^{-1} (vs, νSi–O–Si); and 694 cm^{-1} (vs, νSi–O). EA (SG-Gly–Na^+): C (Exp. 20.052 %), H (Exp. 7.533 %), and N (Exp. 0.214 %).

2.4. Synthesis of non-functionalized silica gel (5: SG).

The sol-gel method is used to carry out a one-pot reaction in the presence of 30 mmol (1.2 g) sodium hydroxide dissolved in 20 mL of distilled water and 6 mL of ethanol. Then, 30 mmol (5.47 mL) of 1,3-chloropropyltrimethoxysilane is added dropwise with vigorous stirring, and the reaction continues for 3 hours at 25°C, following an initial 10 minutes of stirring. The

color gradually changes from colorless to milky, eventually forming a brittle white precipitate. After the reaction is complete, the mixture is covered and left at ambient temperature for two days, then filtered, washed with ethanol and distilled water, ground into a fine powder, and dried for three hours using a rotary evaporator at 75°C. Yield: 1.4 g (66 %). M.p. (decom.) 304°C (light white). ATR-FT-IR (KBr pellet): 1108 and 1027 cm^{-1} (vs, νSi–O–Si); 696 cm^{-1} (vs, νSi–O); 3596 cm^{-1} (s, νSi–OH). EA (SG-OH): C (Exp. 24.352 %) and H (Exp. 8.283 %).

2.5. Capturing Fe^{3+} ions by batch process.

A batch setup is employed to test the Fe^{3+} ion capture ability of the SG-Gly–Na^+ material at T = 25°C (±1°C) and initial concentration C_i = 100 mg/L. A thermostatic mechanical shaker set to 80 rpm is used to vigorously agitate a closed sorption system containing 2 g/L of SG-Gly-Na^+ powder. Following sorption, the supernatant solution is filtered using Whatman No. 41 filter paper. An average of at least three replicate measurements is used to analyze the filtrate solutions.

2.6. Equilibrium studies.

Calculating the equilibrium amount of Fe^{3+} ions adsorbed onto the SG-Gly–Na^+ material is possible. In this case, the percentage capturing Fe^{3+} ions can be calculated as follows:

$$\%\ Capturing\ of\ \text{Fe(III) ion} = \frac{C_i - C_e}{C_i} \times 100\% \qquad (1)$$

C_i and C_e are the initial and the equilibrium concentrations of Fe^{3+} ions in the aqueous solution (mg L^{-1}), respectively.

3. Results and Discussion

3.1. Synthesis of glycine-functionalized silica gel (SG-Gly-Na^+).

The new SG-Gly–Na^+ material is synthesized by reacting Gly–Na^+ (1: Gly = glycine) with 1,3-chloropropyltrimethoxysilane (2: CPTMS) in a 1:1 molar ratio. After appropriate workup, the PTMS-Gly-Na^+ intermediate (3) is isolated as white crystals as described in Scheme 1. After three hours of reaction, almost all chloride functionalities in the compound 2 are displaced by a strong σ-donor hydrogen of the primary amine in compound 1, forming the PTMS-Gly-Na^+ (3). SG-Gly–Na^+(4) is prepared via the condensation-hydrolysis process of the 3. Figure 1a illustrates the formation of SG-Gly–Na^+ as fragile solids and fine powders. The sol-gel synthesis of SG-Gly–Na^+ yields 2.7 g, corresponding to 57% of the theoretical maximum. This moderate yield suggests that while the process is efficient, there may be opportunities for optimization—possibly in the reaction conditions or post-synthesis processing steps—to enhance overall yield. Elemental analysis of SG-Gly–Na^+ shows carbon (C: 20.052%), hydrogen (H: 7.533%), and nitrogen (N: 0.214%). These values confirm the successful incorporation of glycine into the silica matrix. The relatively low nitrogen content suggests that not all glycine molecules are retained in the final material, possibly due to partial decomposition or loss during washing and drying.

The non-functionalized silica gel (5: SG) is prepared in a one-pot reaction using the sol-gel technique. 1,3-Chloropropyltrimethoxysilane is condensed in a solution of NaOH, H_2O,

and EtOH at 25°C. After two days of vigorous stirring, a milky-white powder is produced, as shown in Scheme 2 and Figure 1b. The synthesis yields 1.4 g of non-functionalized silica gel as a white powder, corresponding to a 66% yield. The yield is higher than that of the functionalized SG-Gly–Na^+ synthesis, suggesting that the simpler composition—without glycine and sodium ions—possibly leads to fewer material losses and a more straightforward synthesis process. The decomposition temperature of the non-functionalized silica gel is 304°C, significantly higher than that of the functionalized SG-Gly–Na^+ (240°C). This increased thermal stability is expected, as the non-functionalized silica gel does not contain organic components like glycine, which may lower the decomposition temperature. The high decomposition temperature suggests robust Si–O bonds within the silica network, making it suitable for applications requiring high thermal stability. The elemental analysis results for the non-functionalized silica gel (SG-OH) are: carbon (C: 24.352%) and hydrogen (H: 8.283%).

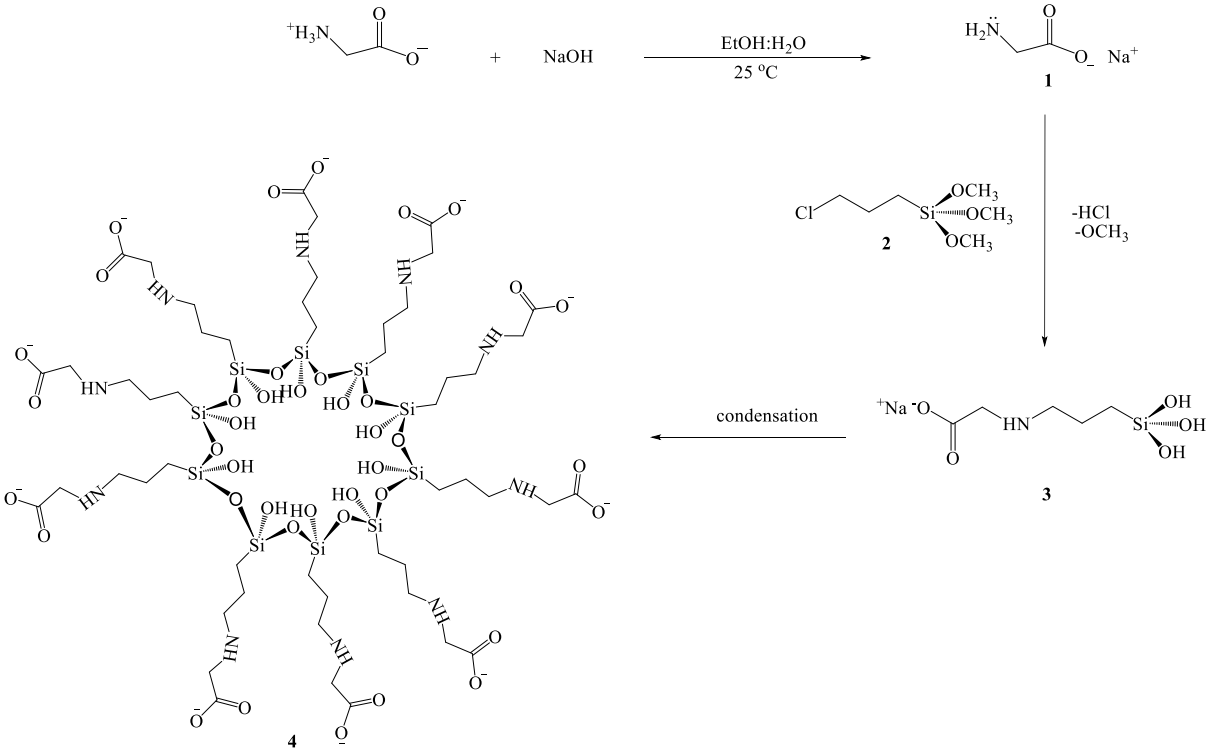

Scheme 1. The SG-Gly–Na^+ (4) reaction equation.

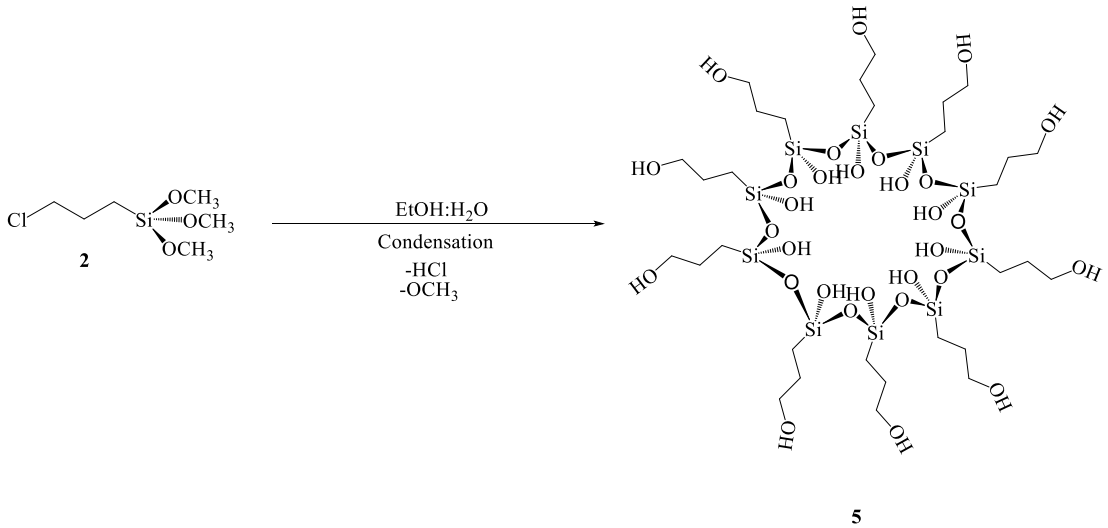

Scheme 2. The SG (5) reaction equation.

(a) **(b)**

Figure 1. The synthesized **(a)** SG-Gly^{-}Na^{+}; **(b)** SG material.

Moreover, the elemental analysis indicates the presence of nitrogen (~0.214%) in the SG-Gly–Na^{+} sample, which is absent in the SG, providing evidence of the incorporation of glycine into the network.

3.2. ATR-IR.

Both SG-Gly–Na^{+}and SG materials are monitored and characterized using ATR-IR spectroscopy. The ATR-IR spectrum of 1,3-chloropropyltrimethoxysilane (2: CPTMS) shows a strong absorption peak at 1075 cm^{-1}, assigned to the Si–O bond [13], and a C–Cl bond deformation at 803 cm^{-1} [14]. The C–H stretching vibrations appear at 2841 and 2944 cm^{-1} (see Figure 2). The ATR-IR spectrum of Gly-Na^{+} (1) exhibits characteristic peaks corresponding to the primary amine (ν-NH2: 3373 and 3342 cm^{-1}) and the carboxylate group (νC=O and νC–O at 1558, 1494, and 1459 cm^{-1}, respectively). The reaction progress between 1 and 2 can be monitored by: (i) the disappearance of the dual primary amine absorption peaks, with the emergence of a single peak for the secondary amine at 3385 cm^{-1} in compound 3, and (ii) the disappearance of the C–Cl deformation band at 803 cm^{-1}. Both observations indicate a successful reaction between 1 and 2, resulting in the formation of 3 (see Figure 2). Additionally, the reaction progress is supported by a gradual decrease in the pH of the solution over time. Moreover, elemental analysis reveals a nitrogen content of 0.214%, further confirming the incorporation of glycine into the SG-Gly–Na^{+} structure.

Figure 3 shows the ATR-IR spectrum of SG-Gly–Na^{+} (4). When compound 3 undergoes hydrolysis and condensation to form SG-Gly–Na^{+} (4), it exhibits two vibrational modes corresponding to the symmetric and asymmetric stretching vibrations of the Si–O and Si–O–Si backbones, located at 1017 cm^{-1}, 1101 cm^{-1}, and 694 cm^{-1}, respectively. Additionally, a new peak at 469 cm^{-1} corresponds to O–Si–O bending vibration modes, confirming the formation of the siloxane (Si–O–Si) network. The peaks associated with the carboxylate group (νC=O and νC–O at 1562 and 1495 cm^{-1}, respectively) appear without significant shifts compared to compounds 1 and 3. Moreover, the peak at 1592 cm^{-1} indicates the wagging bend of the secondary amine (νN–H) [15], while the absorption peak of the secondary amine (ν2° N-H: 3385 cm^{-1}) appears at 3385 cm^{-1}. The low intensity of the peak observed in the 1623–1590 cm^{-1} range, close to the carbonyl region, supports the presence of secondary amine groups rather than primary amines. This is further emphasized by the strong absorption from the Si–O–Si stretching band [16].

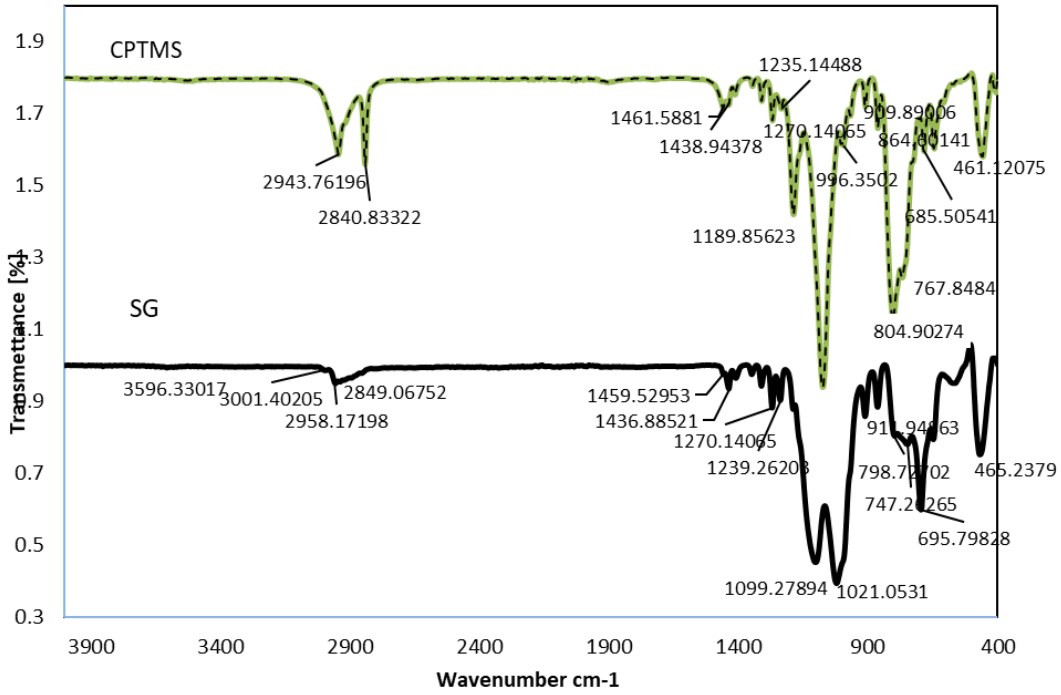

Figure 2. The ATR-IR spectra of 1,3-chloropropyltrimethoxysilane (CPTMS, **2**) and unmodified silica gel (SG, **5**). The spectrum of CPTMS exhibits a strong Si–O stretching vibration at 1075 $cm^{-1}$and a C–Cl deformation band at 803 cm^{-1}, confirming the presence of the chloropropyl functional group. The C–H stretching vibrations appear at 2841 and 2944 cm^{-1}. In contrast, the ATR-IR spectrum of SG (**5**) shows broad O–H stretching vibrations around 3430 cm^{-1} and a bending vibration of adsorbed water at 1631 cm^{-1}. The Si–O–Si asymmetric and symmetric stretching bands appear at 1083 and 800 cm^{-1}, respectively, with a characteristic Si–OH bending peak at 963 cm^{-1}, confirming the typical siloxane network of the silica gel structure.

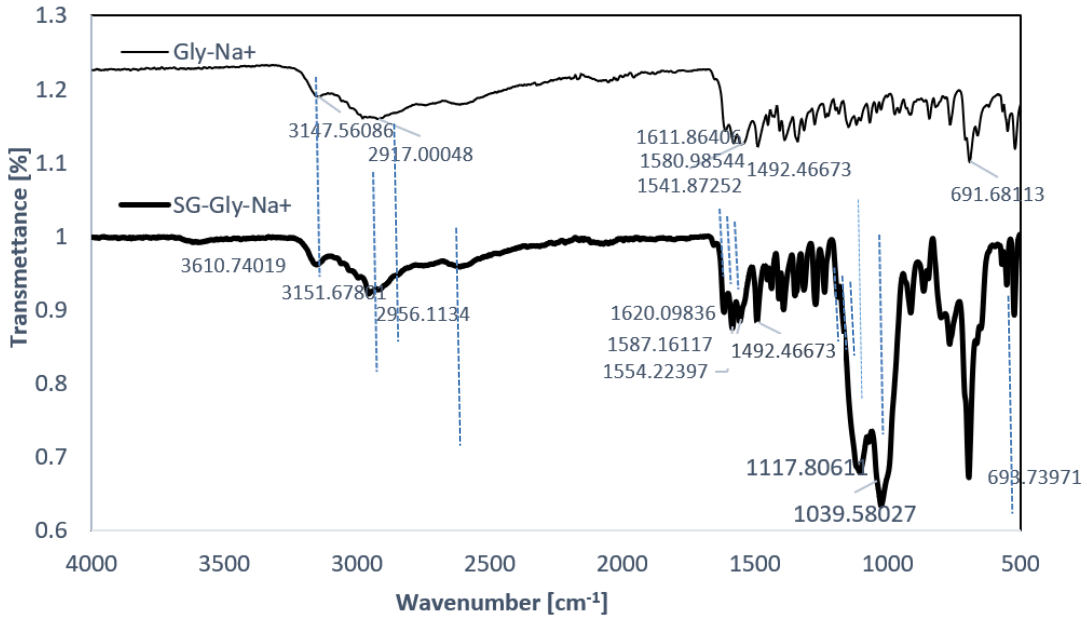

Figure 3. The ATR-IR of $Gly^{-}Na^{+}$ (**1**) and SG-$Gly^{-}Na^{+}$ (**4**). This figure illustrates the successful incorporation of glycine into the silica matrix via the appearance of new peaks at 1017 cm^{-1} and 1101 cm^{-1} (Si–O and Si–O–Si stretches) and 694 cm^{-1} (Si–O bending). The O–Si–O bending mode appears at 469 cm^{-1}, confirming siloxane network formation. Carboxylate stretching bands ($\nu_{C=O}$ at 1562 cm^{-1} and ν_{C-O} at 1495 cm^{-1}) are preserved from $Gly^{-}Na^{+}$, while a secondary amine vibration at 3385 cm^{-1} confirms amine presence in the SG-$Gly^{-}Na^{+}$ structure.

The reaction mechanism of the SG-Gly–Na^{+} material toward iron(III) ions involves chemical interactions between the metal ion and the carboxylate functional groups of the glycinate active sites within SG-Gly–Na^{+}. This coordination occurs through an ion exchange process, wherein the sodium ions (Na^{+}) present in SG-Gly–Na^{+} are replaced by Fe^{3+} ions. To

confirm this mechanism, Gly-Na^+ was reacted with Fe^{3+} to form the [$Fe(Gly^-)_3$] complex. The successful formation of this complex is demonstrated via ATR-IR spectroscopy, as shown in Figure 4. The symmetric and asymmetric stretching vibrations of the carboxylate groups (νC=O and νC–O) shift to higher frequencies, appearing at 1615 and 1582 cm^{-1} (νC=O) and 1504 cm^{-1} (νC–O), compared to those in Gly-Na^+ at 1558 cm^{-1}, 1494 cm^{-1}, and 1459 cm^{-1}, respectively. The separation between asymmetric and symmetric vibrations, Δν(C=O) = 87 cm^{-1} and Δν(C–O) = 45 cm^{-1}, falls below 120 cm^{-1}, which is characteristic of a chelating carboxylate coordination mode [17]. These results confirm that the carboxylate groups bind to Fe^{3+} via the oxygen atoms through an ion exchange process with Na^+.

Furthermore, upon the formation of the [$Fe(Gly^-)_3$] complex, the stretching vibrations of the primary amine shift significantly, appearing at 3242 cm^{-1} and as a broad band at 3414 cm^{-1}, compared to their original positions in Gly-Na^+ (νNH_2: 3373 and 3342 cm^{-1}). The first observed peak at 3242 cm^{-1} is likely overlapped with the stretching vibration of adsorbed water (νO–H). This downward shift (Δν 1°: N–H = 131 and 72 cm^{-1}) to lower frequencies suggests the involvement of the amine group in binding Fe^{3+} ions. From this, it can be concluded that glycinate (Gly^-) acts as a chelating ligand, forming the [$Fe(Gly^-)_3$] complex through both its carboxylate and amine functional groups. However, in the case of glycine immobilized on the silica gel network (SG-Gly–Na^+), the amine group does not appear to participate in the coordination of Fe^{3+}. This implies that the coordination is primarily through the carboxylate sites and that the amine group remains unbound in the SG-Gly–Na^+ structure.

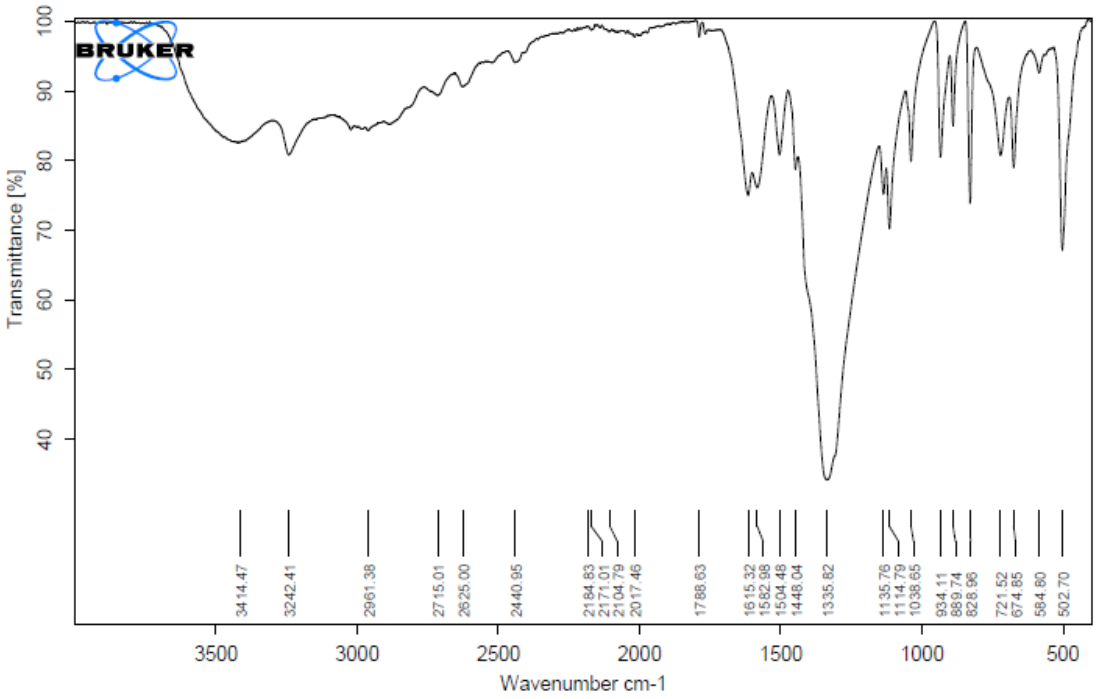

Figure 4. ATR-IR of reaction 1 with Fe^{3+} ion-producing [$Fe(Gly^-)_3$] at pH = 3. The $\nu_{C=O}$ and ν_{C-O} carboxylate bands shift to 1615, 1582, and 1504 cm^{-1}, indicating chelation of Fe^{3+} through oxygen atoms. The Δν values (87 cm^{-1} and 45 cm^{-1}) support a bidentate coordination mode. Significant shifts in amine vibrations (from 3373/3342 cm^{-1} to 3242/3414 cm^{-1}) suggest that primary amine groups also participate in Fe^{3+} coordination in this homogeneous solution-phase complex.

The sorption of Fe^{3+} ions by SG-Gly^-Na^+ material was further confirmed using ATR-IR spectroscopy, as shown in Figure 5. Following sorption, the carboxylate stretching vibrations in SG-Gly^-Fe^{3+} appear at 1590 cm^{-1} ($\nu_{C=O}$) and 1585 cm^{-1} (ν_{C-O}). These bands are

shifted to higher wavenumbers ($\Delta\nu$ = 91 and 78 cm^{-1}, respectively) compared to their positions in SG-Gly^{-}Na^{+}before sorption. This shift indicates successful chemisorption of Fe^{3+} ions via coordination with the carboxylate groups. A peak at 1641 cm^{-1} corresponds to the bending mode of water molecules [17], supporting the presence of hydration around the adsorbed ions. The broad absorption band at 3324 cm^{-1} may arise from the O–H stretching vibrations of surface silanol groups (≡Si–OH) or from adsorbed water molecules on the silica surface. Additionally, the secondary amine N–H stretching band (from compound **4**) appears close to the O–H region and becomes overlapped within the broad band at 3324 cm^{-1}, suggesting possible hydrogen bonding or surface interactions. Notably, the Si–O–Si and O–Si–O vibrational modes remain unchanged, indicating that the silica gel framework retains its structural integrity under the sorption conditions.

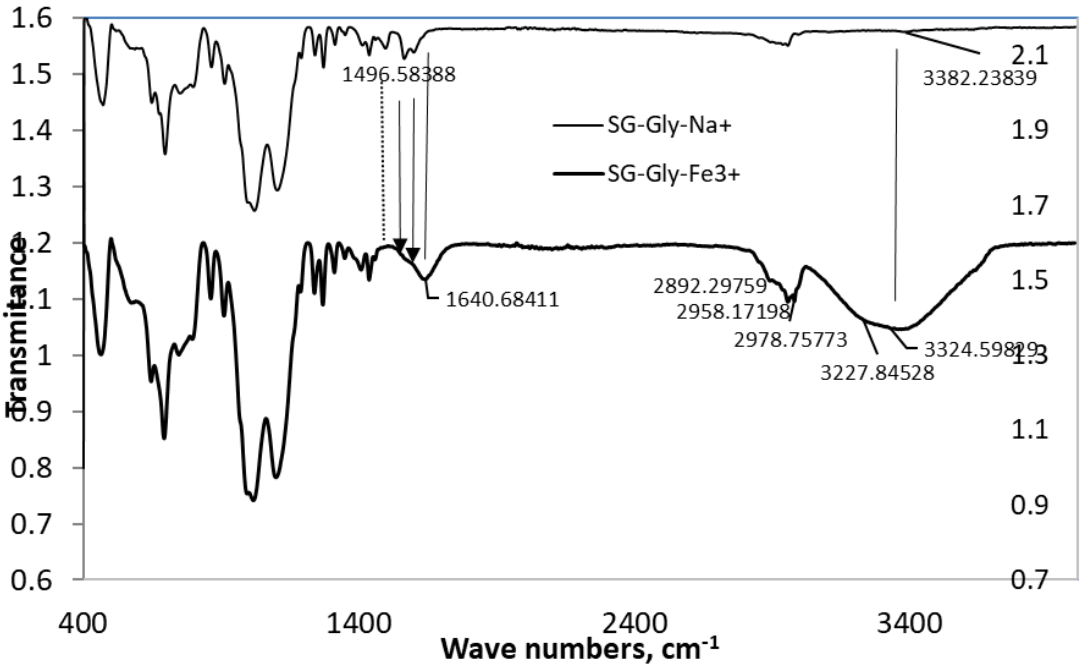

Figure 5. ATR-IR of water SG-Gly^{-}Na^{+} and SG-Gly^{-}Fe^{3+}. Shifts in $\nu_{C=O}$ and ν_{C-O} bands from 1495/1562 cm^{-1} to 1590/1585 cm^{-1} upon Fe^{3+} binding indicate coordination via carboxylate groups. The broadband at 3324 cm^{-1} is attributed to O–H stretching from surface silanols or adsorbed water and overlaps with the N–H stretch, suggesting hydrogen bonding. A peak at 1641 cm^{-1} corresponds to water bending vibrations. The Si–O–Si and O–Si–O peaks remain stable, confirming that the silica framework is structurally intact post-sorption.

3.3. X-ray diffraction.

The X-ray diffraction (XRD) pattern of the synthesized silica gel is presented in Figure 6. The diffractogram exhibits a broad peak centered at 2θ ≈ 21.18° and a narrow peak around 2θ ≈ 7.16°, both of which are characteristic of amorphous silica structures [16, 18]. The broad hump near 2θ = 20°–30° reflects the short-range order typical of amorphous silica, while the low-angle reflection near 2θ = 7° may suggest the presence of some textural or mesostructural ordering. The XRD profiles were analyzed in terms of peak position, relative intensity (I/I_0), peak shape, and full width at half maximum (FWHM) to compare the surface morphology of SG, SG-Gly^{-}Na^{+}, and SG-Gly^{-}Fe^{3+}. Upon comparison, both SG and SG-Gly^{-}Na^{+} show a dominant broad peak around 2θ ≈ 21°, confirming the amorphous nature of the silica network [16, 19]. This structural feature remains evident even after Fe^{3+} sorption, as seen in the SG-Gly^{-}Fe^{3+} pattern, indicating that the silica framework retains its amorphous character throughout the functionalization and adsorption processes. Additionally, comparison with the crystalline Gly^{-}Fe^{3+} complex reveals clear differences, highlighting the distinct structural

environment of the Fe^{3+} ions within the silica-based matrix versus the discrete molecular complex.

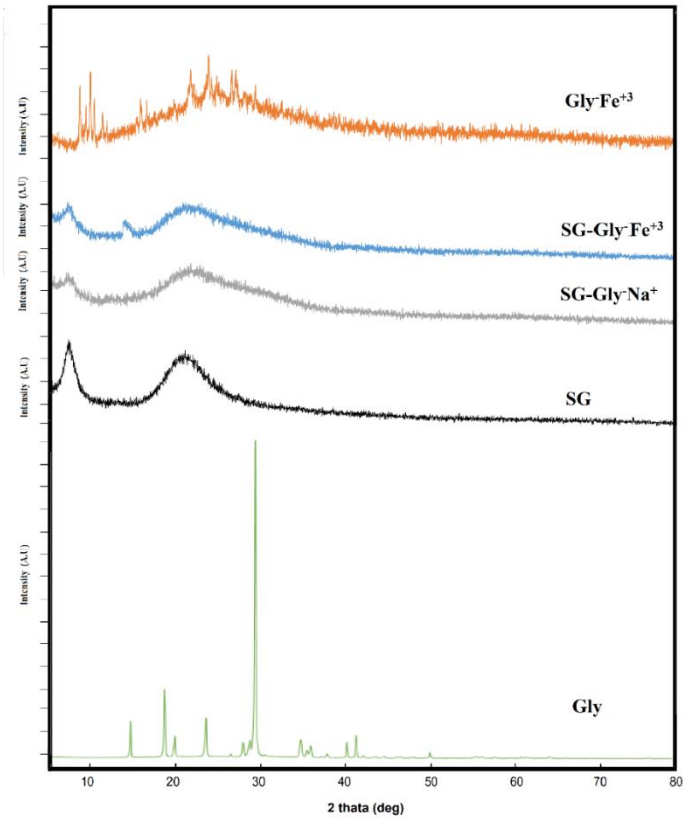

Figure 6. The P-XRD pattern of Gly and Gly-Fe^{3+}, as well as the Silica Xerogel of SG, SG-Gly$^{-}Na^{+}$, and SG-Gly$^{-}Fe^{3+}$.

Following the surface modification of SG and Gly$^{-}Na^{+}$, Figure 6 shows that no significant new diffraction peaks appeared beyond those already present in the pristine SG pattern. The diffraction profiles of SG-Gly$^{-}Na^{+}$ and SG-Gly$^{-}Fe^{3+}$ are largely similar, except for a notable anomalous peak at approximately $2\theta \approx 14°$, which presents an unusual shape and low intensity. This feature may be attributed to the ion exchange between Na^{+} and Fe^{3+}, along with the increased incorporation of Fe^{3+} into the silica matrix, suggesting successful sorption of iron ions by SG-Gly$^{-}Na^{+}$ [20]. Additional evidence of glycine imprinting within the silica structure is observed in the form of a shoulder-like peak around $2\theta \approx 30°$, which correlates with the highest intensity diffraction peak of crystalline glycine. The overall diffraction intensity also decreases from 1681 and 1488 arbitrary units (a.u.) (for SG) to 982.5 and 1097 a.u. (for SG-Gly$^{-}Na^{+}$ and SG-Gly$^{-}Fe^{3+}$), indicating structural or compositional changes in the modified materials. Moreover, subtle shifts in peak positions were observed following functionalization: the diffraction peaks initially located at $2\theta \approx 7.38°$ and 21.22° shifted to $2\theta \approx 7.06°$ and 21.76°, respectively. These shifts suggest local structural reorganization and possible interaction between the silica framework and the incorporated organic moieties or metal ions.

The X-ray diffraction (XRD) pattern of the Gly$^{-}Fe^{3+}$ complex exhibits distinct structural differences compared to SG-Gly$^{-}Na^{+}$ and SG-Gly$^{-}Fe^{3+}$ materials. A key indicator of glycine imprinting within the silica matrix is the presence of a shoulder-like peak at approximately $2\theta \approx 30°$, which correlates with the highest intensity diffraction peak of crystalline glycine. Moreover, a notable decrease in diffraction intensity (from 1681 and 1488 a.u. to 982.5 and 1097 a.u., respectively) suggests modifications in crystallinity and internal structure following iron ion sorption.

The XRD analysis reveals significant structural alterations in the silica gel upon glycine functionalization and subsequent Fe^{3+} incorporation. The broad peak around $2\theta \approx 21°$ and the narrow reflection at $2\theta \approx 7.16°$ confirm the amorphous nature of the silica matrix. In contrast, the emergence of an anomalous peak at $2\theta \approx 14°$, along with peak duplication near $2\theta \approx 21°$ in the SG-Gly^{-}Fe^{3+} pattern, provides compelling evidence of successful ion exchange and glycine-based structural imprinting. Comparison with the Gly–Fe^{3+} complex further highlights the unique features of the SG-Gly^{-}Fe^{3+} material, supporting the hypothesis that the modified silica matrix hosts a distinct coordination environment and framework structure resulting from the interaction between the embedded glycine moieties and Fe^{3+} ions.

3.4. Thermal analysis.

Figure 7 presents the thermogravimetric analysis (TGA) curve of the synthesized SG-Gly^{-}Na^{+} material. The TGA profile reveals two distinct weight loss stages, indicative of the material's thermal decomposition behavior. The first stage, occurring between 350–450 °C, corresponds to the thermal degradation of glycine and other organic moieties covalently anchored to the silica surface. This decomposition is associated with the release of volatile byproducts such as CO_2, NH_3, and other gaseous species containing C, H, N, and O elements. This weight loss confirms the successful organic functionalization of the silica network. The second major weight loss, observed between 450–550°C, is attributed to the decomposition of more thermally resilient organic residues, possibly linked via stronger siloxane or organosilane bonds. This stage reflects the breakdown of more stable organic-silica linkages that persist beyond the initial degradation phase. The total weight loss, remaining under 40% up to 600°C, aligns with the expected composition of SG-Gly^{-}Na^{+} and supports the presence of organic functional groups grafted onto the silica framework. Additionally, the thermal stability up to ~370 °C underscores the robust integration of glycine moieties into the silica matrix before significant thermal decomposition.

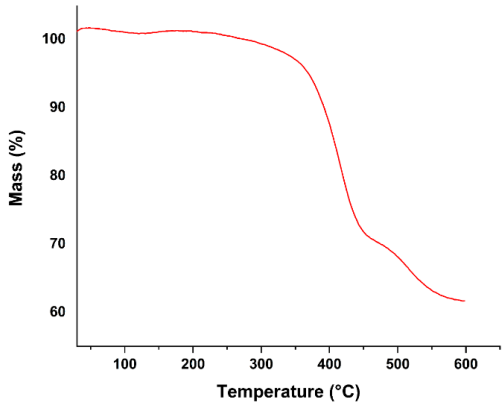

Figure 7. Thermogravimetric analysis (TGA) curve of SG-Gly^{-}Na^{+} material. The TGA profile shows two major weight loss stages. The first occurs between 350–450°C, corresponding to the decomposition of glycine and other covalently bonded organic moieties on the silica surface, releasing volatile products such as CO_2 and NH_3. The second weight loss between 450–550°C indicates the breakdown of more thermally stable organic residues linked through stronger siloxane or organosilane bonds. The overall weight loss remains under 40% up to 600°C, confirming successful organic functionalization and the thermal stability of SG-Gly–Na^{+} up to approximately 370°C.

3.5. SEM and surface morphology.

The surface morphology of SG, SG-Gly–Na^{+}, and SG-Gly–Fe^{3+} was investigated using Scanning Electron Microscopy (SEM). All samples were sputter-coated with gold (Quorum

Q150R) before imaging and analyzed using a high-resolution field emission SEM (FEI QUANTA FEG 450, Netherlands) operating at 30 kV and 20 kV. Figure 8 displays SEM micrographs that reveal notable differences in surface morphology among the samples. The pristine silica gel (SG) exhibits a high degree of particle agglomeration, typical of amorphous silica materials. In contrast, the SG-Gly–Na^+ surface shows flatter regions with non-uniform pore distribution, characterized by regularly shaped spherical pores, indicating successful modification with glycine-sodium groups. Following the sorption of Fe^{3+} ions, the surface morphology of SG-Gly–Fe^{3+} appears largely unchanged, maintaining the porous structure observed in SG-Gly–Na^+. However, Fe^{3+} ions are visibly distributed within the available pores, suggesting that ion exchange between Fe^{3+} and Na^+ ions has occurred at the active sites. This observation supports the proposed sorption mechanism and confirms the structural integrity of the modified silica matrix during the metal ion uptake process.

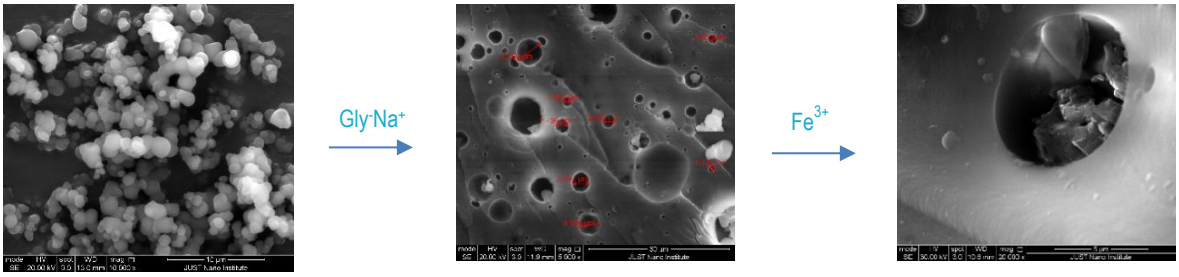

(a) **(b)** **(c)**

Figure 8. SEM micrographs of **(a)** unmodified silica gel (SG), **(b)** glycine-functionalized silica gel **(**SG-Gly$^-$ Na^+), and **(c)** iron-loaded glycine-modified silica gel **(**SG-Gly$^-$$Fe^{3+}$). Image **(a)** shows a significant particle agglomeration characteristic of amorphous silica. Image **(b)** displays a flatter surface morphology with non-homogeneous but regularly shaped spherical pores, indicating successful surface modification with glycine-sodium groups. Image **(c)** reveals that after Fe^{3+} ion sorption, the overall surface structure remains intact while Fe^{3+} ions are visibly distributed within the pores, consistent with an ion exchange mechanism. The preserved porous morphology in SG-Gly$^-$$Fe^{3+}$ confirms the structural stability of the material during sorption.

3.6. Synchrotron XAFS study.

The oxidation state and local coordination environment of Fe in the SG-Gly$^-$$Na^+$ material were investigated using X-ray Absorption Near-Edge Structure (XANES) and Extended X-ray Absorption Fine Structure (EXAFS) spectroscopy. These techniques provide atomic-level insights into the chemical state and bonding characteristics of Fe after ion exchange with Fe^{3+}. The XANES spectrum of SG-Gly$^-$$Fe^{3+}$ exhibits a sharp absorption edge at 7112 eV, identical to that of Fe in the reference SG sample (7112 eV), as shown in Figure 9. The absence of a shift toward lower energies confirms that the oxidation state of Fe remains +3 following incorporation into the SG-Gly$^-$$Na^+$ matrix. This observation suggests that no redox transformation occurs during the sorption process. A very weak pre-edge feature (Peak A) appears at approximately 7112 eV, corresponding to the 1s → 3d quadrupole transition. The intensity of this pre-edge peak in SG-Gly$^-$$Fe^{3+}$ is comparable to those observed in $Fe(NO_3)_3 \cdot 9H_2O$ and Fe_2O_3 reference spectra, both of which are representative of Fe^{3+} species. The low intensity of the pre-edge peak is indicative of octahedrally coordinated Fe^{3+}, consistent with the presence of Fe^{3+} as inner-sphere surface complexes in the SG-Gly$^-$$Fe^{3+}$ material. This interpretation is further supported by comparisons with standard reference materials, including FeO (Fe^{2+}), Fe_2O_3 (Fe^{3+}), and metallic Fe (Fe^0), reinforcing that the sorbed iron exists in the Fe(III) oxidation state and is structurally stabilized within the silica-glycine network as SG-Gly$^-$$Fe^{3+}$ complexes.

These results confirm that glycine incorporated into the SG-Gly⁻Na⁺ matrix does not reduce Fe^{3+} ions to Fe^{2+} or Fe^{0}, contradicting some earlier reports that suggest glycine can act as a reducing agent [9]. In the current study, no evidence of Fe reduction is observed, supporting findings from previous work on iron coordination complexes, which also report the persistence of the Fe^{3+} oxidation state under similar conditions [22, 23]. Figure 10 presents the Fe *K*-edge XANES spectra for Fe incorporated into SG-Gly⁻Na⁺ and pristine SG. The absorption edge positions and spectral features indicate that Fe remains in the +3 oxidation state, with no detectable shift to lower energy that would suggest partial reduction. The spectral characteristics are consistent with Fe^{3+} species, where the oxidation state may lie within the formal range of $0 < \delta \leq +3$, further reinforcing the lack of redox interaction during sorption.

To the best of our knowledge, this is the first report confirming the presence and stability of Fe^{3+} ions within SG and SG-Gly⁻Na⁺ materials post-sorption. Notably, previous studies have not addressed the oxidation state of iron adsorbed on similar silica-based matrices, nor have they explored the potential influence of the support on the redox behavior of Fe. Our findings, therefore, contribute new insight into the redox stability and coordination environment of Fe^{3+} within functionalized silica materials.

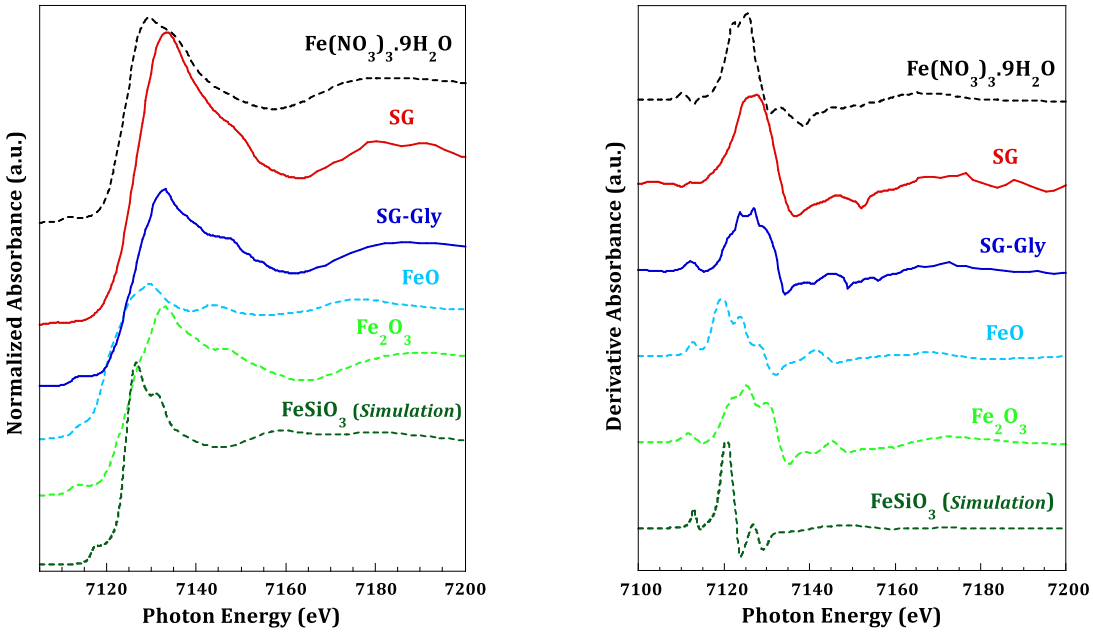

Figure 9. XANES data collected at the Fe K-edge for SG⁻Fe^{3+}, SG-Gly⁻Fe^{3+}, FeO (Fe^{2+}), Fe_2O_3 (Fe^{3+}), $Fe(NO_3)_3.9H_2O$ (Fe^{3+}), and $FeSiO_3$(Fe^{2+}).

EXAFS data were collected at the Fe-K-edge (7112 eV) to characterize the captured Fe^{3+} ion's local atomic and structural environment. The EXAFS signal collected at the Fe K-edge (7112 eV) was k^3 weighted and Fourier transformed on a wave number range of 2-12 $Å^{-1}$ using a Kaiser Basel window function.

The EXAFS signal of the SG-Gly and Fe reference models and their respective ones are shown in Figure 10. It clearly illustrates the domination of Fe(III) when compared with different Fe standard references, such as Fe(0) Metal, Fe(II)O, and $Fe(III)_2O_3$. Moreover, EXAFS data fitting of the SG-Gly sample (Figure 11b) allows interpretation of the different peaks of the FT, attributing the first dominant peak fitted at the interatomic distance of 1.95 Å (1.5 Å at Figure 11b) to oxygen's first neighbor's Fe-O for an average coordination number of 3.4±0.6 atoms. This appears to be much lower than the usual coordination number for Fe(III), wherein the structure of Fe(III)-glycinate complexes was previously investigated [24]. These

findings suggest that Fe(III) was in a tetrahedral coordination environment, involving carboxylates as shown in Figure 10a.

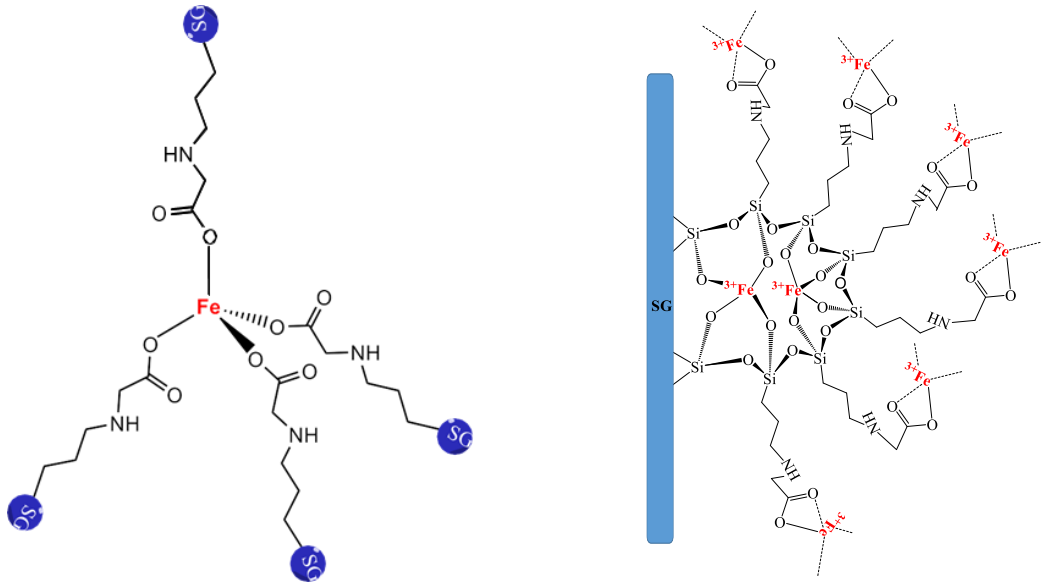

(a) **(b)**

Figure 10. The iron's local atomic and structural environment into **(a)** SG-Gly⁻Fe^{3+}; **(b)** SG-Si-O⁻Fe^{3+}.

The second peak fitted for an average interatomic distance of ~3.25 Å (appearing at 2.8 – 3.0 Å) is assigned to an average number of 7±1 Si backscattering atoms. EXAFS-derived structural parameters around Fe central atoms in SG-Gly⁻Fe^{3+} are listed in Table 1. This pattern could be attributed to SG-Gly⁻Fe^{3+} and/or SG-Si-O⁻Fe^{3+} matching the peak of iron ion binding glycine and silica gel. The seven Si atoms may represent second-shell interactions, where Fe^{3+} is indirectly coordinated to silicon atoms through bridging oxygen atoms (Fe-O-Si linkages) as shown in Figure 10b. This extended coordination is common in silica-supported complexes due to the three-dimensional framework of the silica gel. The silica surface may offer multiple silanols (-SiOH) or siloxane (-Si-O-Si-) groups near the Fe^{3+} ion, contributing to the observed coordination number. This could reflect a distribution of Fe^{3+} species across different binding sites. Therefore, a minor fraction of Fe^{3+} ions might aggregate or interact with silica in ways that increase the apparent Si coordination number. However, the dominant Fe species remains mononuclear and tetrahedrally coordinated as proposed.

The measured Fe-O interatomic distance confirmed the formation of inner-sphere sorption complexes on SG-Gly⁻ surfaces, which have a symmetric Td coordination of Fe ions (see Figure 10). The lower peak intensity of Fe-(O) bonding and higher intensity for Fe-Si bonding of SG-Gly⁻ confirm the role of SiO_2-protected iron ions. These results are found in good agreement with the reported ones [25]. Such coordination is characteristic of iron ions located within the silicate framework, suggesting Si-O-Fe species found in the matrix, as shown in Figure 10.

Table 1. EXAFS-derived structural parameters around Fe central atoms.

Sample	Bond	N (atoms)	R (Å)	σ^2 (Å^2)	ΔE (eV)
SG-Gly⁻Fe^{3+}	Fe-O	3.4±0.6	1.95 ± 0.003	0.0032±0.0005	-1.0±0.5
	Fe-Si	7.1±1.0	3.25±0.004	0.0071±0.0007	2.8± 0.4

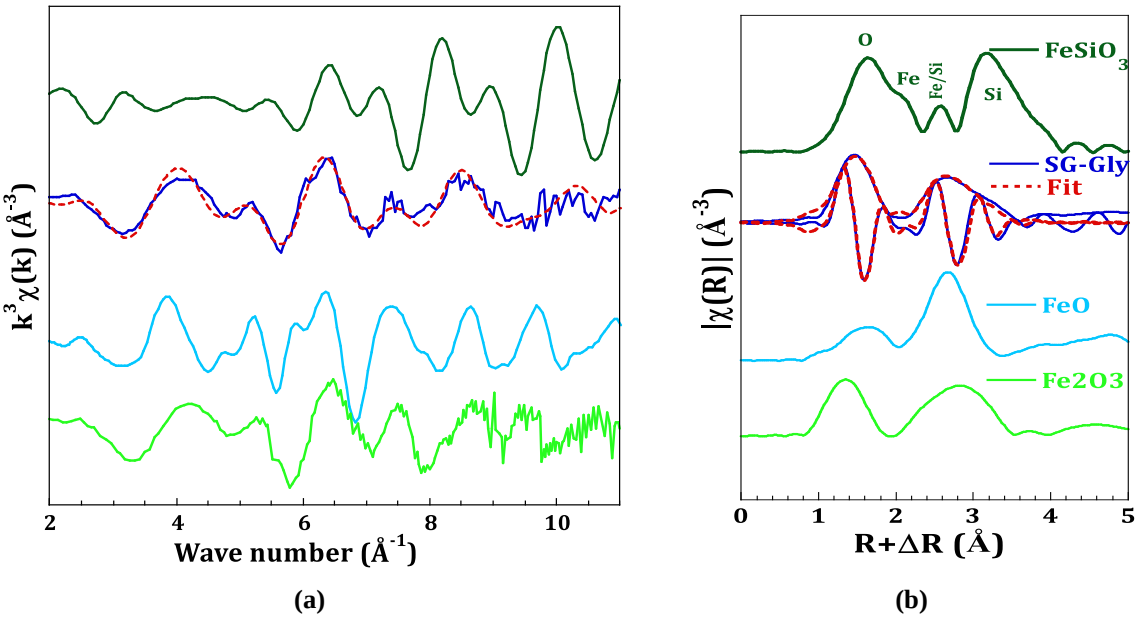

Figure 11. (a) EXAFS k^3 weighted signal collected at the Fe K-edge on the SG-Gly sample compared with Fe reference models; **(b)** Respective Fourier Transforms of the EXAFS signal. Samples are presented with the fitting curves in both *k* and *R* space

3.7. Capturing Fe(III) ions into SG-Gly–Na+ material.

Figure 12 shows the capturing performance of SG-Gly^{-}Na^{+} material toward the Fe^{3+} ion. The batch process started by submersing some SG-Gly^{-}Na^{+} particles (2 g L^{-1}) in the aqueous Fe(III) ion solutions (C_i = 100 mg L^{-1}) at T = 25°C, 80 rpm with pH_i = 3. At this pH in an aqueous solution, Fe(III) is a mixture of Fe^{3+}, $[Fe(OH)]^{2+}$, and $[Fe(OH)_2]^{+}$, depending on Fe(III) concentration, ionic strength, etc. However, this does not impact the sorption behavior. Wherein, the significance of anchoring Gly^{-}Na^{+} into SG enhances the sorption of Fe^{3+} ions by 70 % in contrast with non-functionalized SG (10 %). The Fe^{3+} ion is chemisorbed by carboxylate active sites, forming an inner-sphere complex (SG-Gly^{-}Fe^{3+}). The ion exchange of Fe^{3+} *vs.* Na^{+} cations may take place, which enhances the chemisorption process.

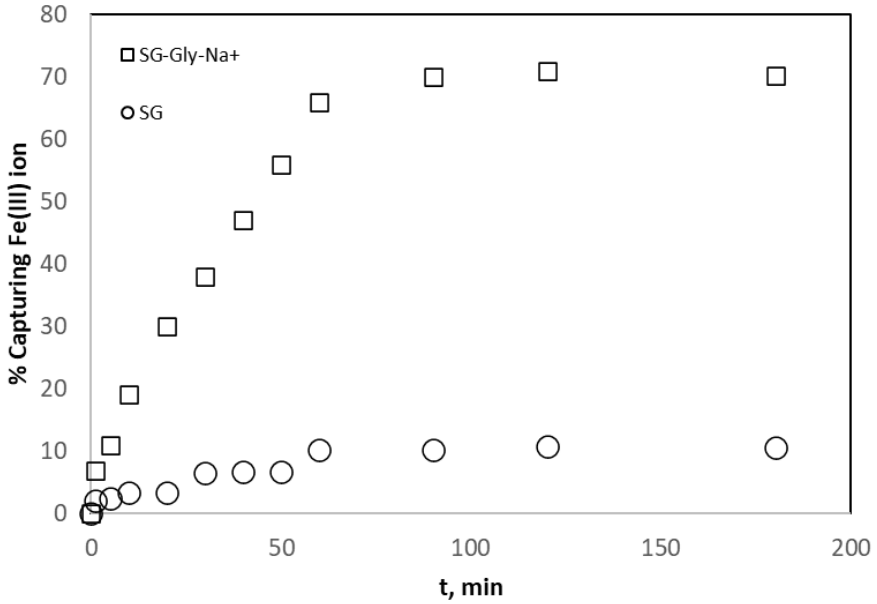

Figure 12. Capturing profile of Fe^{3+} ion into non-functionalized SG *vs.* SG-Gly^{-}Na^{+} material (condition parameters are C_i = 100 mg L^{-1}, T = 25°C, pH_i = 3, 80 rpm, 2 g L^{-1}, 100 – 250 μm).

4. Conclusions

In this study, it has been shown that SG-Gly^{-}Fe^{3+} exhibits an efficiency for capturing and stabilizing Fe^{3+} ions within the matrix network as a monolayer cover. The SG-Gly^{-}Fe^{3+} complex exhibits tetrahedral coordination, with Fe^{3+} ions forming stable inner-sphere bonds via carboxylate groups and Fe-O-Si linkages. EXAFS and ATR-IR confirm robust Fe^{3+} binding and silica matrix stability, with Fe-O and Fe-Si distances of 1.95 Å and ~3.25 Å, respectively. Wherein, the observed Si backscattering reflects second-shell interactions in a Fe-O-Si-like structure, highlighting stable Fe^{3+} incorporation into the silica framework. We believe that SG-Gly^{-}Na^{+} can be used as a potential ion-exchange material for Fe^{3+} ions by 70 % in contrast with non-functionalized SG (10 %), based on the experimental condition parameters.

Author Contributions

Conceptualization, M.A.A. and A.K.H.; methodology, M.A.A.; software, ; validation, M.A.A., A.K.H., and N.A.A.; formal analysis, M.A.A.; investigation, M.A.B.; resources, A.K.H., D.S., and S.S.; data curation, D.S. and S.S.; writing—original draft preparation, M.A.A.; writing—review and editing, M.A.A.; visualization, M.A.A. and N.A.A.; supervision, M.A.A. and A.K.H.; project administration, M.A.A.; funding acquisition, . All authors have read and agreed to the published version of the manuscript.

Data Availability Statement

All data generated or analyzed during this study are included in this published article and its supplementary materials. Additional datasets or raw data used and/or analyzed during the current study are available from the corresponding author upon reasonable request.

Funding

This research received no external funding.

Acknowledgments

Al-Anber gratefully acknowledges the financial support provided by Mutah University – Deanship of Scientific Research – for the financial support provided through the research grant issued under Decision No. 448/2021. Al-Anber would like to extend his thanks to the Synchrotron-light for Experimental Science and Applications in the Middle East (SESAME) in Jordan for performing XAFS Studies.

Conflicts of Interest

The authors declare that they have no competing interests.

References

1. Zaitoun, M.; Al-Anber, M.; Al Momani, I. Sorption and Removal of Aqueous Iron(III) Ion by Tris(2-Aminoethyl)amine Moiety Functionalized Silica Gel. *Int. J. Environ. Anal. Chem.* **2019**, *100*, 1446–1467, https://doi.org/10.1080/03067319.2019.1654466.
2. Majewski, P.; Albrecht, T.; Weber, S. COOH-Functionalisation of Silica Particles. *Appl. Surf. Sci.* **2011**, *257*, 9282–9286. https://doi.org/10.1016/j.apsusc.2011.04.145.

3. Yantasee, W.; Rutledge, R.D.; Chouyyok, W.; Sukwarotwat, V.; Orr, G.; Warner, C.L.; Warner, M.G.; Fryxell, G.E.; Wiacek, R.J.; Timchalk, C.; Addleman, R.S. Functionalized Nanoporous Silica for the Removal of Heavy Metals from Biological Systems: Adsorption and Application. *ACS Appl. Mater. Interfaces* **2010**, *2*, 2749–2758, https://doi.org/10.1021/am100616b.
4. Bi, X.; Lau, R.J.; Yang, K.L. Preparation of Ion-Imprinted Silica Gels Functionalized with Glycine, Diglycine, and Triglycine and Their Adsorption Properties for Copper Ions. *Langmuir* **2007**, *23*, 8079–8086, https://doi.org/10.1021/la7008072.
5. Al-Anber, M.A.; Al-Momani, I.F.; Zaitoun, M.A.; Al-Qaisi, W. Inorganic Silica Gel Functionalized Tris(2-Aminoethyl)amine Moiety for Capturing Aqueous Uranium(VI) Ion. *J. Radioanal. Nucl. Chem.* **2020**, *325*, 605–623, https://doi.org/10.1007/s10967-020-07270-x.
6. Nuengmatcha, P.; Saengsane, N.; Teppaya, N.; Rattanakomon, N.; Nuengmatcha, P. Iron Removal from Synthetic Aqueous Solution Using Amino-Functionalized Commercial Silica Gel as Adsorbent. *J. Appl. Sci.* **2017**, *16*, 1–7, https://doi.org/10.14416/j.appsci.2017.10.s01.
7. Li, Y.; Liu, S. Synthesis of *l*-Glutamic Acid-Containing Silica Gel for the Adsorption and Immobilization of Zn^{2+} in Water. *Monatsh Chem.* **2019**, *150*, 1349–1354, https://doi.org/10.1007/s00706-019-02393-8.
8. Piątek, J.; de Bruin-Dickason, C.N.; Jaworski, A.; Chen, J.; Budnyak, T.; Slabon, A. Glycine-Functionalized Silica as Sorbent for Cobalt(II) and Nickel(II) Recovery. *Appl. Surf. Sci.* **2020**, *530*, 147–299, https://doi.org/10.1016/j.apsusc.2020.147299.
9. Lee, J.; Kim, S.; Mubeen, S.; Mulchandani, A.; Chen, W.; Choa, Y.; Myung, N.V. Synthesis of Gold Nanostructures Using Glycine as the Reducing Agent. *Nanotechnology* **2020**, *31*, 455–601, https://doi.org/10.1088/1361-6528/abaa76.
10. Harfouche, M.; Abdellatief, M.; Momani, Y.; Abbadi, A.; Al Najdawi, M.; Al Zoubi, M.; Aljamal, B.; Matalgah, S.; Khan, L.U.; Lausi, A.; Paolucci, G. Emergence of the first XAFS/XRF beamline in the Middle East: providing studies of elements and their atomic/electronic structure in pluridisciplinary research fields. *J. Synchrotron Radiat.* **2022**, *29*, 1107–1113, https://doi.org/10.1107/S1600577522005215.
11. Ressler, T. WinXAS: A Program for X-ray Absorption Spectroscopy Data Analysis Under MS-Windows. *J. Synchrotron Radiat.* **1998**, *5*, 118-122, https://doi.org/10.1107/s0909049597019298.
12. Rehr, J.J.; Albers, R.C. Theoretical Approaches to X-ray Absorption Fine Structure. *Rev. Mod. Phys.* **2000**, *72*, 621–654. https://doi.org/10.1103/revmodphys.72.621.
13. Launer P. Silicones, silanes and siloxanes. In: Arkles B, Larson GL, editors. *Silicon Compounds: Silanes & Silicones*. 3rd ed. Morrisville, PA: Gelest Inc.; 2013. p. 175–178. ISBN: 978-0-578-12235-9.
14. Wells, A.F. Structural Inorganic Chemistry, 4th Edition; Clarendon Press **1975**.
15. Fontinha, I.R.; Salta, M.M.; Zheludkevich, M.L.; Ferreira, M.G.S. EIS Study of Amine Cured Epoxy-Silica-Zirconia Sol-Gel Coatings for Corrosion Protection of the Aluminium Alloy EN AW 6063. *Port. Electrochim. Acta* **2013**, *31*, 307–319, https://doi.org/10.4152/pea.201306307.
16. Zhang, J.; Ding, T.; Zhang, Z.; Xu, L.; Zhang, C. Enhanced Adsorption of Trivalent Arsenic from Water by Functionalized Diatom Silica Shells. *PLOS ONE* **2015**, *10*, e0123395, https://doi.org/10.1371/journal.pone.0123395.
17. McIntosh, I.M.; Nichols, A.R.L.; Tani, K.; Llewellin, E.W. Accounting for the Species-Dependence of the 3500 cm^{-1} H_2O Infrared Molar Absorptivity Coefficient: Implications for Hydrated Volcanic Glasses. *American Mineralogist* **2017**, *102*, 1677–1689, https://doi.org/10.2138/am-2017-5952ccby.
18. Zong, S.; Wei, W.; Jiang, Z.; Yan, Z.; Zhu, J.; Xie, J. Characterization and Comparison of Uniform Hydrophilic/Hydrophobic Transparent Silica Aerogel Beads: Skeleton Strength and Surface Modification. *RSC Adv.* **2015**, *5*, 55579–55587, https://doi.org/10.1039/c5ra08714g.
19. Sembiring, S.; Situmeang, R.; Sembiring, Z. Synthesis and Characterization of Asphalt Composite Precursors Using Amorphous Rice Husk Silica. *Cerâmica* **2019**, *65*, 194-199, https://doi.org/10.1590/0366-69132019653742497.
20. Guo, Z.; Zhang, D.; Wei, S.; Wang, Z.; Karki, A.B.; Li, Y.; Bernazzani, P.; Young, D.P.; Gomes, J.A.; Cocke, D.L.; Ho, T.C. Effects of Iron Oxide Nanoparticles on Polyvinyl Alcohol: Interfacial Layer and Bulk Nanocomposites Thin Film. *J. Nanopart. Res.* **2010**, *12*, 2415–2426, https://doi.org/10.1007/s11051-009-9802-z.
21. Yamamoto, T. Assignment of Pre-Edge Peaks in K-Edge X-ray Absorption Spectra of 3d Transition Metal Compounds: Electric Dipole or Quadrupole? *X-Ray Spectrometry* **2008**, *37*, 572–584, https://doi.org/10.1002/xrs.1103.

22. Takahara, A.; Higaki, Y.; Hirai, T.; Ishige, R. Application of Synchrotron Radiation X-ray Scattering and Spectroscopy to Soft Matter. *Polymers* **2020**, *12*, 1624, https://doi.org/10.3390/polym12071624.
23. Terzano, R.; Mimmo, T.; Vekemans, B.; Vincze, L.; Falkenberg, G.; Tomasi, N.; Schnell Ramos, M.; Pinton, R.; Cesco, S. Iron (Fe) Speciation in Xylem Sap by XANES at a High Brilliant Synchrotron X-ray Source: Opportunities and Limitations. *Anal. Bioanal. Chem.* **2013**, *405*, 5411–5419, https://doi.org/10.1007/s00216-013-6959-1.
24. Thundathil, R.V.; Holt, E.M.; Halt, L.S.; Watson, K.J. Preparation and Properties of Iron(III)-Amino Acid Complexes. 2. The Crystal and Molecular Structure of Monoclinic Tri-μ_3-Oxo-Triaquohexakis(Glycine)triiron(III) Perchlorate. *J. Am. Chem. Soc.* **1977**, *99*, 1818–1823, https://doi.org/10.1021/ja00448a024.
25. Olimov, K.; Falk, M.; Buse, K.; Woike, T.; Hormes, J.; Modrow, H. X-ray Absorption Near Edge Spectroscopy Investigations of Valency and Lattice Occupation Site of Fe in Highly Iron-Doped Lithium Niobate Crystals. *J. Phys. Condens. Matter.* **2006**, *18*, 5135–5146, https://doi.org/10.1088/0953-8984/18/22/013.

Publisher's Note & Disclaimer